NURBS plasticity: non-associated plastic flow

William M. Coombs[a], Yousef Ghaffari Motlagh[b]

[a]*Department of Engineering, Durham University, Durham, DH1 3LE, UK.*
T: +44 (0) 191 334 2516, F: +44 (0) 191 334 2408, E: w.m.coombs@durham.ac.uk
[b]*Department of Civil and Structural Engineering, University of Sheffield, Sheffield, S1 3JD, UK.*
E: y.ghaffari-motlagh@sheffield.ac.uk

Abstract

This paper extends the non-uniform rational basis spline (NURBS) plasticity framework of Coombs et al. [11] and Coombs and Ghaffari Motlagh [10] to include non-associated plastic flow. The NURBS plasticity approach allows any smooth isotropic yield envelope to be represented by a NURBS surface whilst the numerical algorithm (and code) remains unchanged. This paper provides the full theoretical and algorithmic basis of the non-associated NURBS plasticity approach and demonstrates the predictive capability of the plasticity framework using both small and large deformation problems. Wherever possible errors associated with the constitutive formulation are specified analytically and if not numerical analyses provide this information. The rate equations within the plasticity framework are integrated using an efficient and stable implicit stress update algorithm which allows for the derivation of the algorithmic consistent tangent which ensures optimum convergence of the global out of balance force residual when used in boundary value simulations.

The important extension provided by this paper is that the evolution of plastic strain is decoupled from the yield surface normal. This allows the framework to model more realistic material behaviour, particularly in the case of frictional plasticity models where an associated flow rule is known to significantly overestimate volumetric dilation leading to spurious results. This paper therefore opens the door for the NURBS plasticity formulation to be used for a far wider class of material behaviour than is currently possible.

Keywords:
elasto-plasticity, constitutive modelling, non-associated flow, non-uniform rational basis spline (NURBS), stress integration, finite-element analysis

1. Introduction

Constitutive models that provide incremental relationships between stress and strain are essential for boundary value analysis of engineering problems. Within this, one of the most common classes of material behaviour is elasto-plasticity where the elastic region of

stress space is bounded by a yield surface. On this yield surface the material will undergo elasto-plastic material behaviour and countless yield envelopes have been proposed since the works of Tresca [21] and von Mises [15]. However, the form of the yield function impacts on the stress integration algorithm which is required to convert the rate form of the plasticity equations into an incremental form that can be used in boundary value simulations (using the finite element method for example). This issue was overcome by the non-uniform rational basis spline (NURBS) plasticity framework of Coombs et al. [11] and Coombs and Ghaffari Motlagh [10] which allowed an smooth isotropic yield envelope to be integrated using the same numerical algorithm. However, [11] and [10] were limited to the case of associated plastic flow where the form of the yield surface governs both the yielding of the material and the evolution of plastic strains. This limits the form of material behaviour that can be predicted and, in the case of frictional plasticity models, leads to a significant overestimation of volumetric dilation. This paper overcomes this limitation by decoupling the evolution of plastic strains from the yield surface normal leading to a non-associated plastic flow constitutive framework.

In this paper we do not attempt to review all of the constitutive models available in the literature, instead an interested reader is refereed to the work of Yu [24] for a general review of constitutive models. In the specific area of NURBS plasticity, beyond the work of [10, 11], the only other paper that the authors are aware of is that of Coelho et al. [3] who construct NURBS response surfaces in biaxial strain and stress space based on curve fitting to experimental data. This is quite different to the approach of [10, 11], and that advocated in this paper, where a NURBS yield envelope is constructed and then used within a conventional plasticity formulation. This approach provides a constitutive formulation which is valid for generalised, six-component, stress and strain space.

The NURBS plasticity formulation is combined with an implicit predictor-corrector stress integration algorithm [22] to provide an incremental relationship between stress and strain. Several papers have compared different stress integration algorithms and, as with the vast array of constitutive models, in this paper we do not attempt to review them. In this case the interested reader is refereed to the works of Anandarajah [1] and Safaei et al. [17], amongst others. The reasons for adopting an implicit algorithm in this paper are twofold: (i) they rigorously enforce the consistency conditions at the updated stress state (and in the case of NURBS plasticity, throughout the process) and (ii) allow for the derivation of the algorithmic consistent tangent that ensures asymptotic quadratic convergence of the global residual when used within a boundary value simulation.

The layout of the paper is as follows, Section 2 provides the theoretical framework for hardening non-associated flow NURBS-based plasticity, including the definition of the NURBS surface and the non-associated flow rule, isotropic hardening through the movement of control points, the form of stress integration used and the technique of energy mapped stress that allows us to interpret the stress integration method as a geometric projection. Section 3 provides details on the numerical implementation including the backward Euler stress integration process and the algorithmic consistent tangent. Numerical

examples are presented in Section 4 and, finally, conclusions are drawn in Section 5.

The majority of the paper is presented in tensor form using index notation, the notable exception is the numerics that are presented in matrix-vector form for ease of implementation. Due to the geometric nature of the method presented in this manuscript, the majority of the paper is presented in principal stress and strain space with the following ordering of the principal stresses

$$\sigma_1 \geq \sigma_2 \geq \sigma_3,$$

with tensile stresses taken as positive. Note that although the equations are presented in principal stress space we can do this without loss of generality of the final result as the principal quantities are simply transferred back to generalised quantities at the end of the algorithm. Generalised, 6-component, stress and strain quantities are denoted using $\hat{(\cdot)}$.

2. Non-associated flow NURBS plasticity

This section provides the essential equations required for an isotropically hardening NURBS surface with non-associated plastic flow. There is significant overlap between the theory presented here and that of Coombs et al. [11] (for perfect plasticity with associated flow) and Coombs and Ghaffari Motlagh [10] (for isotropic hardening with associated flow), however the repetition is retained for the sake of clarity and to provide a self-contained formulation. For more detailed information on the construction of NURBS-based surfaces see the work of Piegl and Wayne [16] and the paper of Coombs et al. [11] for the particular case of perfect plasticity yield envelopes.

A general NURBS surface can be expressed as

$$S_k(\xi,\eta) = \sum_{i=0}^{n}\sum_{j=0}^{m} R_{i,j}(\xi,\eta)(C_k)_{i,j}, \tag{1}$$

where k is the physical index, C_k are the control point positions and n and m are the number of control points in the local ξ and η directions[1]. The NURBS basis functions, $R_{i,j}$, are given by

$$R_{i,j}(\xi,\eta) = \frac{N_{i,p}(\xi)N_{j,q}(\eta)w_{i,j}}{\sum_{k=0}^{n}\sum_{l=0}^{m} N_{k,p}(\xi)N_{l,q}(\eta)w_{k,l}}, \tag{2}$$

where $N_{i,p}$ and $N_{j,q}$ are the p^{th} and q^{th}-degree B-spline basis functions (see [12, 16], amongst others), ξ and η are the local positions within the knot vectors and $w_{i,j}$ are the weights associated with the control points.

[1]Note that the total number of control points used to define the surface is $n \times m$.

2.1. NURBS-based yield envelopes

Starting from the equation for a NURBS surface (1), a NURBS-based yield envelope [10, 11] can be expressed as

$$f = \Big(\sigma_i - S_i(\xi, \eta)\Big)(S_{,\sigma})_i = 0, \tag{3}$$

where $(S_{,\sigma})_i$ is the surface outward normal (that is, the partial derivative of S with respect to stress) and σ_i the principal stress state. The yield surface separates stress space into two regions: an elastic region where $f < 0$ and an inadmissible region where $f > 0$. The boundary between these two regions ($f = 0$) is used to identify the point of yielding and stress states on this surface will undergo elasto-plastic deformation. The outward normal to the yield envelope can be obtained through the cross product of the two local derivatives

$$(S_{,\sigma})_i = (S_{,\eta} \times S_{,\xi})_i = \epsilon_{ijk}(S_{,\eta})_j(S_{,\xi})_k, \tag{4}$$

where ϵ_{ijk} is the Levi-Civita tensor[2]. See [16] for efficient algorithms for the calculation of the derivatives of the NURBS surface with respect to the local coordinates. Figure 1 (i) shows a bi-quadratic spherical NURBS surface with the form

$$f = \sigma_i\sigma_i - r_y^2 = 0,$$

where r_y is the radius of the yield envelope. The control points used to define the surface are shown by the red points and different surfaces can be obtained by moving the positions of the control points and/or modifying the basis functions, $R_{i,j}$. Figure 1 (ii) also shows a number of outward normals, $(S_{,\sigma})_i$, to the spherical yield surface.

The number of control points required to define a NURBS plasticity yield surface will depend on the form of the yield function. The number of control points needed for some widely used yield envelopes are:

- von Mises: open ended cylinder, quadratic NURBS curve in the deviatoric direction to define the circular cross section using 8 control points combined with a straight line in the hydrostatic direction using a minimum of 2 control points - 16 control points in total;
- Tresca: prismatic regular hexagon, linear NURBS curve in the deviatoric direction to define the hexagonal cross section using 6 control points combined with a straight line in the hydrostatic direction using a minimum of 2 control points - 12 control points in total;

[2] $\epsilon_{ijk} = 0$ if $i = j$, $j = k$ or $k = i$, $\epsilon_{ijk} = 1$ for even permutations of i, j and k and $\epsilon_{ijk} = -1$ for odd permutations of i, j and k.

- Drucker-Prager frictional cone: quadratic NURBS curve in the deviatoric direction to define the circular cross section using 8 control points combined with a straight line in the hydrostatic direction using a minimum of 2 control points - 16 control points in total; and
- Mohr-Coulomb frictional cone: linear NURBS curve in the deviatoric direction to define the irregular hexagonal cross section using 6 control points combined with a straight line in the hydrostatic direction using a minimum of 2 control points - 12 control points in total;

However, it may be necessary to use higher order NURBS surfaces in order to be able to avoid numerical issues with the stress integration algorithm, especially in the case of yield envelopes with corners [10, 11] (see Section 4.1 for more details for the Drucker-Prager and Mohr-Coulomb yield surfaces). It is also possible to reduce the number of control points by only defining the yield surface over a single sextant of stress space, where $\sigma_1 \geq \sigma_2 \geq \sigma_3$, as is done in this manuscript and in the work of Coombs and Ghaffari Motlagh [10]. For example, the number of control points required to define a spherical yield surface in all sextants of stress space is 45 whereas if it is defined in a single sextant only 15 points are required [10].

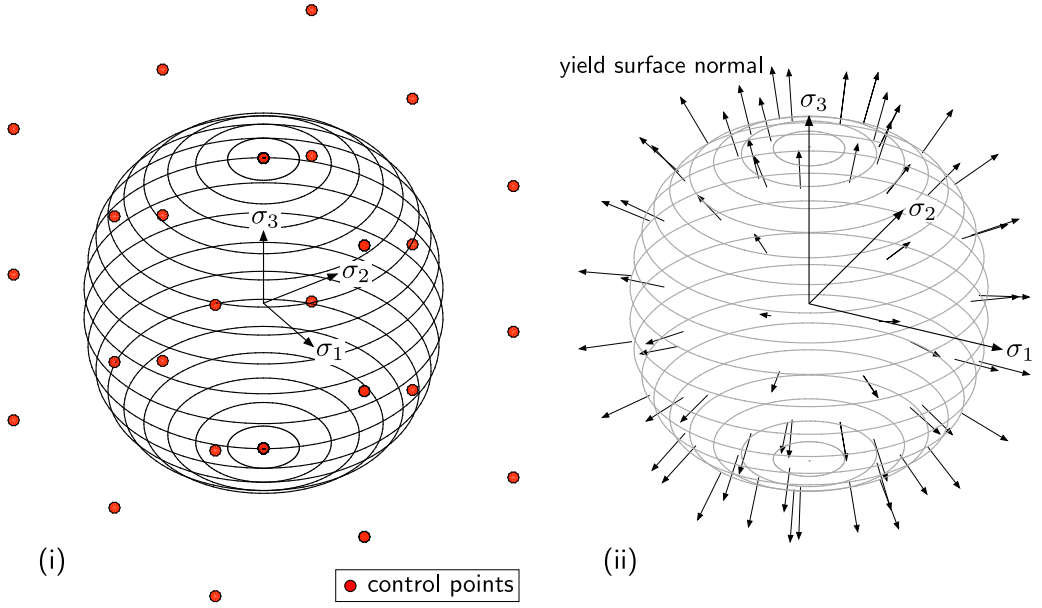

Figure 1: Spherical NURBS surface: (i) yield surface and control point net where the control points are shown by the red-shaded circles and (ii) yield surface with outward normals, $(S,_\sigma)_i$, shown.

For associated flow plasticity theory the outward normal to the yield surface also pro-

vides the flow direction controlling the evolution of plastic strains, that is

$$\dot{\varepsilon}_i^{\mathrm{p}} = \dot{\gamma}(S_{,\sigma})_i, \tag{5}$$

where $\dot{\gamma}$ is the scalar plastic multiplier rate (or consistency parameter). This plastic multiplier rate must satisfy the Kuhn-Tucker-Karush consistency conditions

$$f(\sigma_i, \varepsilon_i^{\mathrm{p}}) \leq 0, \qquad \dot{\gamma} \geq 0 \qquad \text{and} \qquad f(\sigma_i, \varepsilon_i^{\mathrm{p}})\dot{\gamma} = 0, \tag{6}$$

where the yield envelope is a function of plastic strain, $\varepsilon_i^{\mathrm{p}}$, to allow for hardening/softening of the surface. These conditions enforce that the material must either be on the yield surface undergoing elasto-plastic deformation ($f = 0$ and $\dot{\gamma} \geq 0$) or inside the yield surface with purely elastic behaviour ($f \leq 0$ and $\dot{\gamma} = 0$).

2.2. Non-associated flow

In the case of non-associated flow the evolution of plastic strains is decoupled from the spatial gradient of the yield envelope. The plastic strains evolve according to

$$\dot{\varepsilon}_i^{\mathrm{p}} = \dot{\gamma}(g_{,\sigma})_i, \tag{7}$$

where $(g_{,\sigma})_i$ is the gradient of the plastic potential surface.

Previous attempts to extend the NURBS plasticity framework to include non-associated flow have directly specified the flow direction at the control points rather than specifying the geometry of a plastic potential surface (see Coombs [5]). However, when specifying the flow direction at the control points, it is only possible to recover associated flow over the entire yield surface if there is no coupling between the local knot coordinates (ξ, η). One example is the prismatic von Mises yield surface

$$f = \rho - \rho_y = 0, \tag{8}$$

where the deviatoric stress is $\rho = \sqrt{2J_2}$, $J_2 = \frac{1}{2}(s_i s_i)$, $s_i = \sigma_i - \frac{1}{3}\sum_{k=1}^{3}\sigma_k$ and ρ_y is the deviatoric radius of the yield surface. When defined using NURBS plasticity, this surface combines a circle in the ξ (deviatoric) direction with a line in the η (hydrostatic) direction. In this case the radius of the yield surface is not dependent on the η value. However, if we introduce a hydrostatic dependency and extend the von Mises surface to that of Drucker-Prager (D-P) [14], with the form

$$f = \rho + \beta(\zeta - \zeta_a) = 0, \tag{9}$$

the deviatoric and hydrostatic directions are coupled and we loose the ability to recover associated plastic flow over the entire yield surface. In (9) $\zeta = \frac{1}{\sqrt{3}}\sum_{k=1}^{3}\sigma_k$ is the hydrostatic stress, $\beta = \tan(\phi)$ is the opening angle of the cone, ϕ is the friction angle, $\zeta_a = c\sqrt{3}\cot(\phi)$ is the location of the cone's tensile apex and c is the material's cohesion.

Before moving onto the proposed formulation, the error associated with defining the direction of plastic flow at the control points is investigated for the D-P yield surface with a friction angle of $\phi = \pi/9$ (20° degrees) and a cohesion of 0Pa. The NURBS yield surface was defined over the hydrostatic range of $\zeta \in [-2, -1]$Pa using the following knot vectors

$$\Xi_\xi = \{0,0,0,1,1,2,2,3,3,4,4,4\} \qquad \text{and} \qquad \Xi_\eta = \{0,0,1,1\},$$

and weights

$$w_\xi = \{1, 2^{-\frac{1}{2}}, 1, 2^{-\frac{1}{2}}, 1, 2^{-\frac{1}{2}}, 1, 2^{-\frac{1}{2}}, 1\} \qquad \text{and} \qquad w_\eta = \{1,1\},$$

with a linear and quadratic bases in the hydrostatic (local η) and deviatoric (local ξ) directions, respectively. The direction of plastic flow was defined using the approach of Coombs [5] as

$$(g_{,\sigma})_k = \sum_{i=0}^{n}\sum_{j=0}^{m} R^g_{i,j}(\xi,\eta)\big((G_{,\sigma})_k\big)_{i,j}, \tag{10}$$

where $(G_{,\sigma})_k$ are the flow directions at the control points and the NURBS basis functions $R^g_{i,j}(\xi,\eta)$ are calculated in the same way as (2). The flow direction was defined using the following knot vectors

$$\Xi^g_\xi = \{0,0,0,1,1,2,2,3,3,4,4,4\} \qquad \text{and} \qquad \Xi^g_\eta = \{0,0,1,1\},$$

and weights

$$w^g_\xi = \{1,1,1,1,1,1,1,1,1\} \qquad \text{and} \qquad w^g_\eta = \{1,1\},$$

where the weights in the ξ direction have been modified to exactly recover associated plastic flow for a von Mises yield surface. As with the yield surface geometry, the flow direction has linear and quadratic bases in the hydrostatic (local η) and deviatoric (local ξ) directions, respectively.

The control points positions and associated flow directions for the D-P surface were arranged as shown in Figure 2. In all cases the flow directions at the control points had a radial deviatoric direction with the appropriate hydrostatic component for the specified friction angle such that the vector was normal to the cone in the hydrostatic direction (as shown in Figure 2 (i)).

Figure 3 (i) shows the variation in the error of the non-associativity of the plastic flow direction with the deviatoric local position on the yield surface, where the error is defined as

$$e_f = 1 - \frac{(S_{,\sigma})_i (g_{,\sigma})_i}{||(S_{,\sigma})_j|| \cdot ||(g_{,\sigma})_k||} \quad \in [0,2], \tag{11}$$

where $||(\cdot)||$ denotes the L2-norm of $(\cdot)$. The plastic flow direction was calculated using (10) and the normal to the yield surface using (4). Note that Figure 3 (i) only shows the

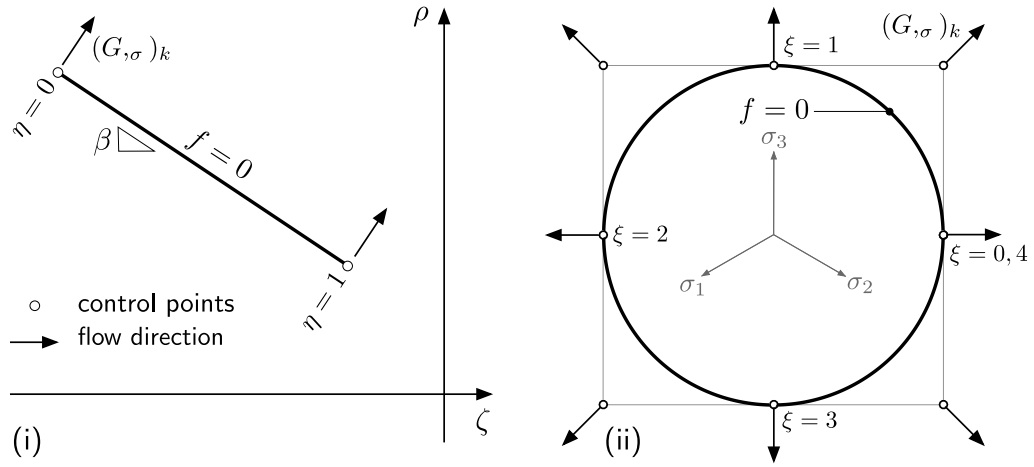

Figure 2: Control point positions and flow directions for a portion of a D-P yield surface: (i) ζ versus ρ and (ii) deviatoric sections through the yield surface.

variation of the error in the ξ direction as the error does not vary in the hydrostatic local direction, η. There is zero error (recovering associated plastic flow) when the control points coincide with the yield surface whereas the error is maximum at the control point local positions that do not coincide with the surface. This error is due to the coupling between the ξ and η directions and increases with an increasing angle of friction, ϕ, as shown in Figure 3 (ii). In all cases the maximum error is located at $\xi = 0.5,\ 1.5,\ 2.5$ and 3.5 and reduces to zero as $\phi \to 0$.

The error in the flow direction is due to the presence of the cross product in (4) meaning that it is not possible to specify the flow direction at the control points and guarantee the recovery of associated plastic flow. That is, even when attempting to recover associated flow, in general

$$(S_{,\eta} \times S_{,\xi})_k \neq \sum_{i=0}^{n} \sum_{j=0}^{m} R^g_{i,j}(\xi, \eta) \big((G_{,\sigma})_k \big)_{i,j} \tag{12}$$

where

$$(S_{,(\cdot)})_k = \sum_{i=0}^{n} \sum_{j=0}^{m} \frac{\partial R_{i,j}(\xi, \eta)}{\partial (\cdot)} (C_k)_{i,j} \tag{13}$$

and $(\cdot)$ refers to ξ or η, as required. It is only possible to recover associated flow over the entire yield surface when the form of the yield function in the ξ and η directions are independent. For example, for the cylindrical von Mises surface the yield radius (in the ξ direction, for example) does not depend on η parametric coordinate but this is not the case for the Drucker-Prager yield envelope where the yield radius varies with η.

In this paper we adopt a more conventional approach, in terms of plasticity theory, and

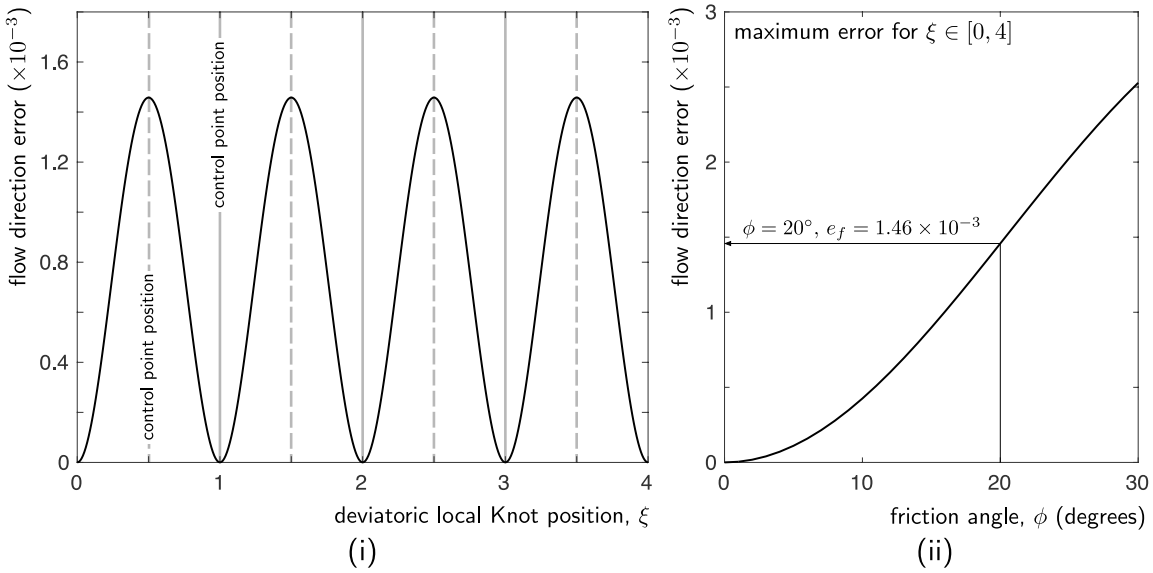

Figure 3: Error in the direction of plastic flow when specifying the flow direction at the control points: (i) variation with ξ for $\phi = 20°$ and (ii) maximum error with friction angle with $\phi \in [0, 30]$ degrees.

specify the geometry of the plastic potential surface using control points. In the case of associated plastic flow the plastic potential control point positions coincide with those used to define the geometry of the yield surface. The gradient of the plastic potential surface therefore given by

$$(g_{,\sigma})_i = (g_{,\eta} \times g_{,\xi})_i = \epsilon_{ijk}(g_{,\eta})_j(g_{,\xi})_k, \tag{14}$$

where $g(\xi, \eta)$ is the plastic potential surface

$$g_k(\xi, \eta) = \sum_{i=0}^{n}\sum_{j=0}^{m} R^g_{i,j}(\xi, \eta)(G_k)_{i,j} \tag{15}$$

and G_k are control point coordinates that control the shape of the surface. Note that it is not necessary to have the same basis functions from the direction of plastic flow as used to describe the geometry of the yield surface however it is assumed that a single set of control points control the form of both the yield, S_k, and plastic potential, g_k, surfaces.

2.3. Isotropic hardening

Consistent with the work of Coombs and Ghaffari Motlagh [10], in this paper the yield surface is allowed to expand or contract isotropically according to the level of inelastic straining at a material point, such that

$$C_k = h(\varepsilon^{\mathrm{p}}_i)C^0_k, \tag{16}$$

where the superscript $(\cdot)^0$ denotes the original control point coordinates and $h(\varepsilon_i^{\mathrm{p}})$ controls the expansion/contraction of the control points. For linear isotropic hardening the incremental evolution of h is given by

$$h(\Delta\varepsilon_i^{\mathrm{p}}) = h_n + \alpha||\Delta\varepsilon_i^{\mathrm{p}}||, \tag{17}$$

where $h_n = h\big((\varepsilon_n^{\mathrm{p}})_i\big)$ is the value of the hardening function from the previously converged state and α controls the hardening/softening rate and equals zero in the case of perfect plasticity. Initially the hardening parameter is taken to be unity, that is $h_0 = 1$.

2.4. Stress integration

As with the other NURBS plasticity papers [10, 11], we use an implicit elastic predictor, plastic corrector scheme. The starting point for the stress integration algorithm is the previously converged, or initial, stress state, σ_i^n and hardening parameter, h_n. This state is then subjected to a strain increment, $\Delta\varepsilon_i$, giving an elastic trial stress state of

$$\sigma_i^t = \sigma_i^n + \Delta\sigma_i, \qquad \text{where} \qquad \Delta\sigma_i = D_{ij}^{\mathrm{e}}\Delta\varepsilon_j \qquad \text{and} \qquad \sigma_i^n = D_{ij}^{\mathrm{e}}(\varepsilon_n^{\mathrm{e}})_j. \tag{18}$$

D_{ij}^{e} is the linear elastic stiffness matrix and $(\varepsilon_n^{\mathrm{e}})_j$ is the elastic strain from the previously converged, or initial, state. This trial stress state should be checked against the yield criteria for the material under consideration and if it exceeds to yield envelope then it must be corrected back onto an appropriate stress state on the yield surface. This *return* stress state, σ_i^r, is give by

$$\sigma_i^r = \sigma_i^t - \Delta\sigma_i^{\mathrm{p}}, \qquad \text{where} \qquad \Delta\sigma_i^{\mathrm{p}} = D_{ij}^{\mathrm{e}}\Delta\varepsilon_j^{\mathrm{p}} \tag{19}$$

and $\Delta\epsilon_j^{\mathrm{p}} = \Delta\gamma(g_{,\sigma}\,)_j$ is the plastic strain increment and $\Delta\gamma$ the incremental plastic multiplier. Once the incremental plastic multiplier has been obtained the updated elastic strain is given by

$$(\varepsilon_{n+1}^{\mathrm{e}})_i = (\varepsilon_n^{\mathrm{e}})_i + \Delta\varepsilon_i - \Delta\varepsilon_i^{\mathrm{p}}, \tag{20}$$

and the updated hardening parameter, h, from (17). The remaining question is how to obtain the incremental hardening parameter, $\Delta\gamma$, or the return stress state, σ_i^r, such that the other quantities can be determined? In this paper we adopt a closest point projection (CPP) implicit stress integration algorithm to arrive at the updated stress state. This corresponds to the minimisation [18] of

$$\big(\sigma_i^r - \sigma_i^t\big)C_{ij}^{\mathrm{e}}\big(\sigma_j^r - \sigma_j^t\big), \tag{21}$$

with respect to the return stress σ_i^r whilst satisfying the Kuhn-Tucker-Karush consistency conditions (6), where $C_{ij}^{\mathrm{e}} = (D_{ij}^{\mathrm{e}})^{-1}$ is the elastic compliance matrix. An important point which is often overlooked it that despite this process being referred to as a CPP, the return stress is not the closest point geometrically in standard stress space, but rather the stress

that minimises (21). The only case where the CPP is the geometric closest point on the yield surface from the trial stress state is when the Poisson's ratio is zero and $C^{\mathrm{e}}_{ij} = E^{-1}\delta_{ij}$, where E is the Young's modulus and δ_{ij} the Kronecker delta tensor[3]. However, in this paper we adopt the non-associated flow version of energy-mapped ς_i space (EMSS) [7, 13] to reduce this CPP minimisation to the problem of finding the point on the yield envelope that the normal to the plastic potential surface passes through when intersecting with a trial point outside of the surface. The use of EMSS converts (21) to

$$\frac{1}{E}\big(\varsigma_i^r - \varsigma_i^t\big)\big(\varsigma_i^r - \varsigma_i^t\big) = \big(\sigma_i^r - \sigma_i^t\big)C^{\mathrm{e}}_{ij}\big(\sigma_j^r - \sigma_j^t\big) \tag{22}$$

essentially removing the influence of Poisson's ratio, ν, when finding the energy-mapped return stress state ς_i^r. The following transformation converts between conventional and energy-mapped stress space

$$\varsigma_i = T_{ij}\sigma_j, \qquad \text{where} \qquad T_{ij} = \Big(\sqrt{1-2\nu} - \sqrt{1+\nu}\Big)/3 + \delta_{ij}\sqrt{1-\nu}. \tag{23}$$

This mapping leads to a squashing and a stretching of the yield surface in the hydrostatic and deviatoric directions respectively, as shown in Figure 4 (i) for a spherical yield surface with $\nu = 0.2$ and $\nu = 0.4$. Once the closest point solution in energy-mapped stress space has been found, the solution can be transformed back to conventional stress space. For a NURBS yield surface we only need to map the control point coordinates for the yield, (C_k), and plastic potential, (G_k), surfaces into energy-mapped space, the rest of the NURBS information remains unchanged.

3. Numerical implementation

Consistent with the perfect plasticity associated plastic flow implementation of Coombs et al. [11], here we use a coarse initial subdivision algorithm to provide the initial starting point for a backward Euler (bE) implicit stress integration process. This is to provide an initial estimate for the local positions within the knot vectors, ξ and η in (3) that act as the primary unknowns in the CPP problem (in addition to the updated hardening parameter). The rest of the section is focused on the implicit stress integration algorithm and the derivation of the algorithmic consistent tangent. However, before focusing on the stress integration algorithm we first propose a new method to determine if the material is undergoing elastic or elasto-plastic deformation.

[3]Note, there may be some special forms of non-linear elasticity where the Poisson's ratio goes to zero for certain stress (or strain) states. However, in order for the return state to be the geometrically closest point on the yield surface, the Poisson's ratio would need to be zero over the entire return path, not just at the instantaneous point on the yield surface.

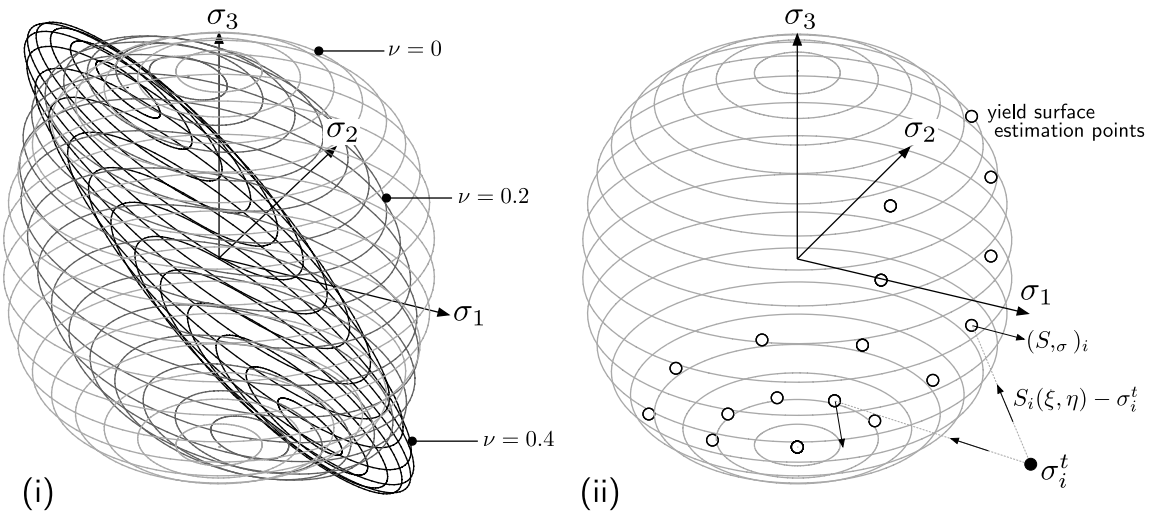

Figure 4: Spherical NURBS surface: (i) yield surface in energy-mapped stress space for three values of Poisson's ratio, ν (modified from [11]) and (ii) points used to estimate the yield function value in one sextant of stress space.

3.1. Yield function estimate

Determining the return stress state on the NURBS surface is only required for stress states undergoing elasto-plastic deformation. However, the yield function for NURBS plasticity (3) requires the return stress state and associated outward normal, therefore in previous NURBS plasticity approaches even for elastic stress states the appropriate return state on the yield surface must be determined. In this paper we propose an alternative technique to predict if the material is undergoing elasto-plastic deformation without determining the return stress state.

The distance between the trial point and a point on the NURBS surface in the direction of the yield surface outward normal, $(S_{,\sigma})_i$, is

$$k_d = \Big(S_i(\xi,\eta) - \sigma_i^t\Big)(S_{,\sigma})_i. \tag{24}$$

In the case of a convex surface, if the trial stress state, σ_i^t, is inside or on the yield surface then $k_d \geq 0$ for all points, $S_i(\xi,\eta)$, on the NURBS yield envelope. However, if $k_d < 0$ for any (ξ,η) then the trial stress state is outside of the yield surface. It is not possible to check that all points on the NURBS surface. Instead a parametric grid of (ξ,η) points are checked where the locations are evenly distributed within that local knot coordinates, that is

$$\xi_d = (\xi_{\min} : \Delta\xi : \xi_{\max}) \qquad \text{and} \qquad \eta_d = (\eta_{\min} : \Delta\eta : \eta_{\max}),$$

where $\Delta\xi = (\xi_{\max} - \xi_{\min})/(n_d - 1)$, $\Delta\eta = (\eta_{\max} - \eta_{\min})/(n_d - 1)$ and n_d is the number of

points considered in each direction. These trial knot locations are shown in Figure 4 (ii) by the white-filled circles in a single sextant of principal stress space for a spherical yield surface. The trial stress state outside of the yield surface is also shown by the black-filled circle as are the vectors used in (24) for two of the trial yield surface points.

3.2. Subdivision algorithm

In this paper we adopt an implicit bE algorithm to determine the updated local position on the yield surface, (ξ, η), and new size of the surface, controlled by h. In order to start of the Newton process of the bE algorithm an initial estimate of the return position and the hardening parameter. Consistent with the work of Coombs et al. [11], a coarse subdivision process is used for the initial estimate of ξ and η whereas, consistent with [10], the previous value of the hardening parameter provides the starting point for h.

The trial local position on the frozen yield surface (that is, $h = h_n$) for the implicit algorithm is selected finding the minimum

$$e_d = 1 - \frac{(\varsigma_i^t - {}^{\varsigma}S_i)({}^{\varsigma}S_{,\varsigma})_i}{||\varsigma_i^t - {}^{\varsigma}S_i|| \cdot ||({}^{\varsigma}S_{,\varsigma})_i||} \quad \in [0, 2], \tag{25}$$

for an initial set of candidate points on the yield surface, where ${}^{\varsigma}S_i$ and ${}^{\varsigma}g_i$ are the energy-mapped yield and plastic potential surfaces. See [11] for details of the subdivision algorithm used to determine the candidate points on the yield surface.

3.3. Implicit stress integration

The energy-mapped stress space bE stress integration algorithm contains three unknowns

$$\{x\} = \{\xi \qquad \eta \qquad h\}^T \tag{26}$$

which satisfy the following residuals

$$\{r\} = \left\{(\varsigma_i^t - \varsigma_i^n)({}^{\varsigma}g_{,\xi})_i \qquad (\varsigma_i^t - \varsigma_i^n)({}^{\varsigma}g_{,\eta})_i \qquad h - \tilde{h}\right\}^T = \{0\}. \tag{27}$$

The tangent directions to the plastic potential surface, $({}^{\varsigma}g_{,\xi})_i$ and $({}^{\varsigma}g_{,\eta})_i$, are obtained through taking the derivative of the energy mapped plastic potential surface with respect to the local coordinates

$$({}^{\varsigma}g_{,(\cdot)})_k = \sum_{i=0}^{n}\sum_{j=0}^{m} \frac{\partial R_{i,j}^g(\xi, \eta)}{\partial(\cdot)} ({}^{\varsigma}G_k)_{i,j}, \tag{28}$$

where $(\cdot)$ is ξ or η depending on the required derivative.

The first two residuals in (27) ensure that the return path in EMSS is in the direction of the energy mapped plastic flow rule and the third that the hardening function has reached

a stationary value at the update stress state, where

$$\tilde{h} = h_n + \alpha||\Delta\varepsilon_i^{\mathrm{p}}|| \qquad \text{and} \qquad \Delta\varepsilon_i^{\mathrm{p}} = C_{ij}^{\mathrm{e}} T_{jl}^{-1}(\varsigma_l^t - \varsigma_l^n). \tag{29}$$

In the above equation $\Delta\sigma_i^{\mathrm{p}} = T_{jl}^{-1}(\varsigma_l^t - \varsigma_l^n)$ is the plastic stress increment over the stress return path. The unknowns are updated through a standard Newton-Raphson process

$$\{\delta x^k\} = -\left[\frac{\partial r}{\partial x}\right]^{-1}\{r^{k-1}\} \qquad \text{and} \qquad \{x^k\} = \{x^{k-1}\} + \{\delta x^k\}, \tag{30}$$

where k denotes the Newton-Raphson iteration number. The derivatives required for the Jacobian matrix, $[\partial r/\partial x]$, are provided in Appendix B. As with the algorithm for associated flow perfect plasticity, the stress return path for NR procedure described in this paper starts and remains in the yield envelope. This leads to inherently stable stress numerics as it eliminates one of the issues associated with bE stress integration, namely the form of the yield function outside of the yield surface and its impact on the efficiency and stability of the stress return process. For example, inappropriately constructed yield equations can contain local minima and/or spurious auxiliary surfaces outside of the true yield envelope which can trap a returning stress state.

3.4. Algorithmic consistent tangent

Specification of the algorithmic consistent tangent allows for asymptotic quadratic convergence of the global out of balance force residual [19]. The tangent is first constructed in principal stress space and then transformed into six-component stress space using the principal directions associated with the trial elastic strain state (see Appendix A for details). Following the approach of [4], we can linearise the constitutive model into the following form

$$\underbrace{\begin{bmatrix} [C^{\mathrm{e}}] + \Delta\gamma[g_{,\sigma\sigma}\,] & \{0\} & \{g_{,\sigma}\,\} \\ -\{\Delta\tilde{h}_{,\sigma}\,\}^T & 1 & -\Delta\tilde{h}_{,\Delta\gamma} \\ \{S_{,\sigma}\,\}^T & f_{,h} & 0 \end{bmatrix}}_{[A^{alg}]^{-1}} \begin{Bmatrix} \{d\sigma\} \\ dh \\ d\Delta\gamma \end{Bmatrix} = \begin{Bmatrix} \{d\varepsilon_t^{\mathrm{e}}\} \\ 0 \\ 0 \end{Bmatrix}, \tag{31}$$

where the derivatives are determined at the updated stress state. $\Delta\tilde{h}$ is the incremental form of the hardening function, and in the case of linear isotropic hardening

$$\Delta\tilde{h} = \alpha||\Delta\varepsilon_i^{\mathrm{p}}||. \tag{32}$$

The derivative of the flow direction with respect to stress is

$$(g_{,\sigma\sigma}\,)_{ij} = \frac{\partial(g_{,\sigma}\,)_i}{\partial\xi}\frac{\partial\xi}{\partial\sigma_j} + \frac{\partial(g_{,\sigma}\,)_i}{\partial\eta}\frac{\partial\eta}{\partial\sigma_j}. \tag{33}$$

The derivatives of the local knot coordinates with respect to stress can be obtained from the inversion of the Jacobian matrix linking the local NURBS coordinates with the principal stress directions, that is

$$[J] = \Big[(S,_{\xi})_i \quad (S,_{\eta})_i \quad (S,_{\sigma})_i \Big]. \tag{34}$$

The normal to the NURBS surface, $(S,_{\sigma})_i$ provides the third direction, orthogonal to the tangent vectors, in the transformation. The derivatives associated with the hardening function are

$$(\Delta\tilde{h},_{\sigma})_i = \alpha \frac{(\Delta\varepsilon^{\mathrm{p}})_j}{||\Delta\varepsilon^{\mathrm{p}}_k||} \Delta\gamma (g,_{\sigma\sigma})_{ij} \qquad \text{and} \qquad \Delta\tilde{h},_{\Delta\gamma} = \alpha \frac{(\Delta\varepsilon^{\mathrm{p}})_i}{||\Delta\varepsilon^{\mathrm{p}}_k||} (g,_{\sigma})_i. \tag{35}$$

The derivative of the yield function with respect to h is

$$f,_h = -(S,_h)_i (S,_{\sigma})_i. \tag{36}$$

Multiplying both sides of (31) by $[A^{alg}]$, allows us to obtain the principal components of the consistent tangent, $[D^{\mathrm{alg}}]$, as

$$\begin{Bmatrix} \{d\sigma\} \\ dh \\ d\Delta\gamma \end{Bmatrix} = \begin{bmatrix} [D^{\mathrm{alg}}] & \{A^{alg}_{12}\} & \{A^{alg}_{13}\} \\ \{A^{alg}_{21}\}^T & A^{alg}_{22} & A^{alg}_{23} \\ \{A^{alg}_{31}\}^T & A^{alg}_{32} & A^{alg}_{33} \end{bmatrix} \begin{Bmatrix} \{d\varepsilon^{\mathrm{e}}_t\} \\ 0 \\ 0 \end{Bmatrix}. \tag{37}$$

The plasticity model presented in this paper has been expressed in principal components. It is therefore necessary to detail the mapping of this model into generalised 6-component space. The equations to convert the stress and strain measures into 6-component space are given in Appendix A, the appendix also details the transformation of the algorithmic (or elasto-plastic) stiffness matrix and the shear components of the algorithmic consistent tangent stiffness matrix. A pseudo-code for the isotropically hardening non-associated flow NURBS plasticity model is given in Figure 5 that details fully the steps required in calculating the updated stress state and hardening parameter.

4. Numerical simulations

This section provides material point and boundary value simulations to demonstrate the performance of the constitutive model and the numerical stress integration algorithm described in the previous sections. However, before the numerical examples are presented we first need to define the NURBS plasticity models.

4.1. Non-associated flow plasticity models

This section provides the NURBS and control point information for the two plasticity models used in the numerical analysis presented in this paper, namely the D-P and Mohr-

1. INPUT: physical ($\{\varepsilon^t\}$, E, ν, h_n) & NURBS information.

   (a) Transform the trial elastic strain, $\{\varepsilon^t\}$, into its principal components and store the associated eigenvectors.

   (b) Calculate the principal (elastic) trial stress, $\{\sigma^t\} = [D^{\mathrm{e}}]\{\varepsilon^t\}$.

   (c) Calculate the control point positions with $h = h_n$.

   (d) Transform the trial stress, $\{\sigma^t\}$, the control point locations and the control point flow directions to energy mapped stress space, (23).

   (e) Determine the value of the yield function based on the procedure given in Section 3.1.

   (f) IF $f >$ tol (*elasto-plastic behaviour*)

      i. Determine the closest point between the trial stress state, $\{\varsigma^t\}$, and the non-associated flow hardening NURBS surface in energy mapped stress space, also obtaining h_{n+1}, based on the bE stress integration algorithm given in Section 3.3;
      ii. transform the return stress state, $\{\varsigma_{cp}\}$, back to conventional stress space;
      iii. calculate the updated elastic strain, $\{\varepsilon^{\mathrm{e}}_{n+1}\} = [D^{\mathrm{e}}]^{-1}\{\sigma_{n+1}\}$; and
      iv. determine the algorithmic consistent tangent matrix, $[D^{a\,\mathrm{lg}}]$, from (37).

   (g) ELSE (*elastic behaviour*)

      i. updated stress equal to the trial stress, $\{\sigma_{n+1}\} = \{\sigma^t\}$;
      ii. updated elastic strain equal to the trial strain, $\{\varepsilon^{\mathrm{e}}_{n+1}\} = \{\varepsilon^t\}$;
      iii. algorithmic tangent equal to the elastic tangent, $[D^{alg}] = [D^{\mathrm{e}}]$; and
      iv. maintain the original hardening parameter, $h_{n+1} = h_n$.

   (h) END IF

   (i) Transform the principal components (updated stress, elastic strain and consistent tangent) back to generalised space using the eigenvectors stored at step (a) - see Appendix A.

2. OUTPUT: $\{\sigma_{n+1}\}$, $\{\varepsilon^{\mathrm{e}}_{n+1}\}$, h_{n+1} and $[D^{alg}]$

Figure 5: Pseudo-code for the non-associated flow isotropically hardening NURBS constitutive model.

Coulomb (M-C) yield surfaces.

4.1.1. Drucker-Prager

The majority of the NURBS information for the D-P yield surface has already been given in Section 2.2. However, the D-P yield surface (9) contains a tensile apex which poses an issue for the stress return algorithm presented in this paper as the derivatives of the NURBS surface are undefined at this point. Here we follow the same approach as Coombs et al. [11] and Coombs and Ghaffari Motlagh [10] and locally round the apex, as shown in Figure 6 with $\zeta_a = 0$. The yield surface is shown in both hydrostatic versus deviatoric stress space and principal stress space for both the original and rounded surfaces. The knot vector and associated control point weights for the grey curve shown in Figure 6 (i) are

$$\Xi_\eta = \{0, 0, 0, 1, 1, 2, 2, 2\} \qquad \text{and} \qquad w_\eta = \{1, 1, 1, \cos(\vartheta/2), 1\}.$$

This knot and weight vector replaces those defined in Section 2.2 for the η direction. The radius of the rounding curve can be obtained from the point where the true and rounded curves depart, point C in Figure 6 (i), that is

$$R = \zeta_{\mathsf{C}} \frac{\tan(\phi)}{\cos(\phi)}, \tag{38}$$

where $\zeta_{\mathsf{C}} < \zeta_a$ and the arc angle is $\vartheta = \pi/2 - \phi$. The hydrostatic locations of points D and E can be subsequently obtained from ζ_{C} and R, where point D lies on the intersection between the original yield curve and a line of constant hydrostatic pressure from the tensile limit of the rounded surface. It is clear from Figure 6 (i) that introducing rounding at the apex of the yield surface generates a region were stress states should be undergoing elastic behaviour or located on the true yield surface that are actually outside of the NURBS surface and therefore inadmissible. However, the maximum hydrostatic error due to the rounding is [10]

$$\text{error} = (\zeta_a - \zeta_{\mathsf{C}}) \left(1 + \frac{\beta}{\cos(\phi)}\right),$$

which can be controlled through setting an appropriate value of ζ_{C}. It is also important to note that the degree of rounding shown in Figure 6 is for visualisation purposes only and is in excess of that used in the numerical analyses.

The ξ-direction knot vectors and control point weights for both the yield and the plastic potential surfaces defined in a single sextant of stress space are

$$\Xi_\xi = \{0, 0, 0, 1, 1, 1\} \qquad \text{and} \qquad w_\xi = \{1, 2^{-\frac{1}{2}}, 1\},$$

where the η-direction information is given above. Combining these gives the thick grey and black dashed curves shown in Figure 6, where $\beta_g = \tan(\psi)$ is the opening angle of the plastic potential surface and $\psi \in [0, \phi]$ is the dilation angle.

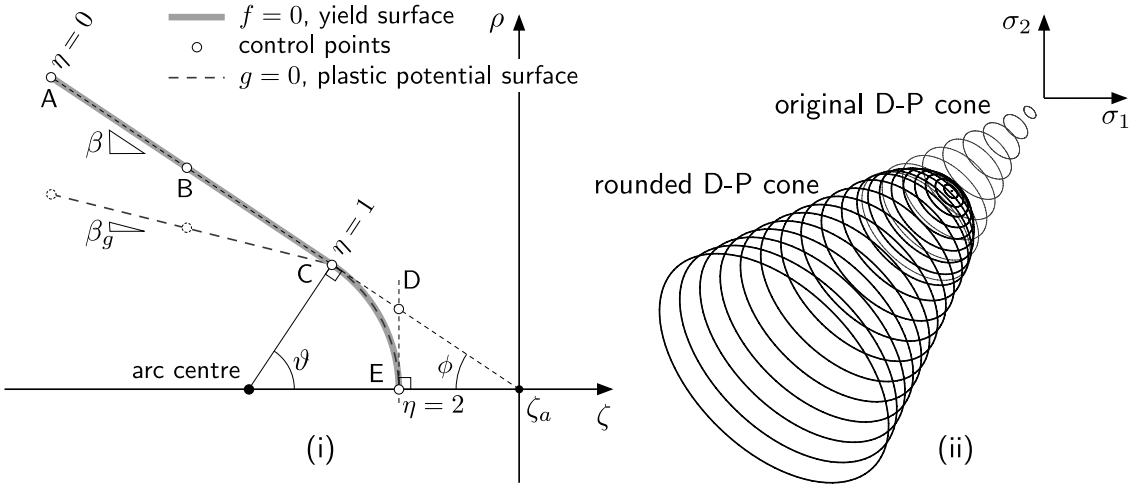

Figure 6: Drucker-Prager yield surface in: (i) hydrostatic, ξ, versus deviatoric, ρ, stress space and (ii) principal stress space showing both the rounded and original cones (note that the degree of rounding is for visualisation purposes only and is in excess of that used in the numerical analyses).

4.1.2. Mohr-Coulomb

The M-C yield surface can be defined as

$$f = k\sigma_3 - \sigma_1 - \sigma_c \qquad \text{where} \qquad k = \frac{1+\sin(\phi)}{1-\sin(\phi)} \qquad \text{and} \qquad \sigma_c = 2c\sqrt{k}. \tag{39}$$

c and ϕ are the cohesion and the friction angle of the material, respectively. In this paper the M-C yield surface is represented using a bi-quadratic NURBS surface with a locally rounded tensile apex using the same approach as for the D-P surface. The M-C yield surface also is only C^0 continuous at both the compression and extension meridians and this will cause issues for the stress integration algorithm which requires the first derivative of the yield surface with respect to stress. We therefore introduce local rounding into the yield surface around these two meridians.

Figure 7 (i) shows a deviatoric section through the NURBS M-C yield surface (thick grey solid line) and the true M-C yield surface (thin black dashed line) in one sextant of stress space. In the figure, the deviatoric radius has been normalised by the yield radius on the compression meridian and the normalised radius on the extension meridian is given by

$$\bar{\rho}_e = \frac{2+k}{2k+1}, \tag{40}$$

in the case of $\phi = 20^\circ$, $\bar{\rho}_e = 0.795$. Both of the meridians of the NURBS surface have been rounded by the same length, δ, where θ_e and θ_c are the arc angles for the extension and

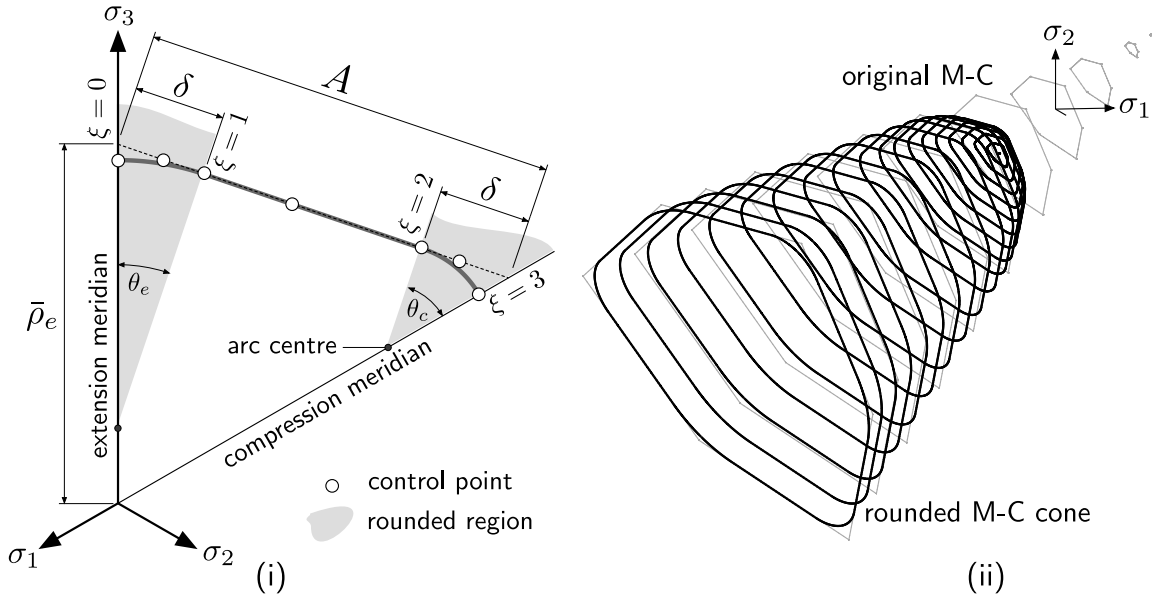

Figure 7: Mohr-Coulomb: (i) normalised deviatoric section through the yield surface and (ii) rounded yield surface in principal stress space (note that the degree of rounding is for visualisation purposes only and is in excess of that used in the numerical analyses).

compression meridians, given by

$$\theta_e = \frac{\pi}{2} - \arcsin\left(\frac{\bar{\rho}_e\sqrt{3}}{2A}\right) \qquad \text{and} \qquad \theta_c = \frac{\pi}{2} - \arcsin\left(\frac{\sqrt{3}}{2A}\right) \tag{41}$$

with $A = \sqrt{\bar{\rho}_e^2 - \bar{\rho}_e + 1}$. The deviatoric section is constructed using seven control points as shown in Figure 7 (i) and the knot vectors for the yield surface defined in a single sextant of stress space are

$$\Xi_\xi = \{0, 0, 0, 1, 1, 2, 2, 3, 3, 3\} \qquad \text{and} \qquad \Xi_\eta = \{0, 0, 0, 1, 1, 2, 2, 2\},$$

and weights are

$$w_\xi = \{1, \cos(\theta_e/2), 1, 1, 1, \cos(\theta_c/2), 1\} \qquad \text{and} \qquad w_\eta = \{1, 1, 1, \cos(\vartheta/2), 1\}.$$

This results in 35 control points being required to define the M-C yield surface in a single sextant of stress space. The NURBS (black line) and true (thin grey line) M-C yield surfaces are shown for all sextants of stress space in Figure 7 (ii), where, as with the D-P surface, the rounding has been exaggerated for visualisation purposes.

The maximum normalised deviatoric radius error at the compression or extension

meridian is given by

$$e_{(\cdot)} = \delta \left(\frac{1}{\sin(\theta_{(\cdot)})} - \frac{1}{\tan(\theta_{(\cdot)})} \right), \tag{42}$$

where the subscript $(\cdot)$ can be e or c for the extension of compression meridians, respectively. Figure 8 (i) shows the variation of the normalised error versus local knot position for $\phi = 0°$, $10°$, $20°$, $30°$ and $40°$. In all cases the maximum error is located at the compression meridian ($\xi = 3$) and in the special case of zero friction angle both the compression and extension meridians have the same maximum error. In this case the M-C surface reduces to the Tresca yield surface; a regular prismatic hexagonal yield surface aligned with the hydrostatic axis. As the friction angle increases the error at the compression meridian increases whereas the error at the extension meridian reduces, this is clearly shown in Figure 8 (ii) where the error at the compression/extension meridian is reported for $\phi \in [0, 40]$ degrees.

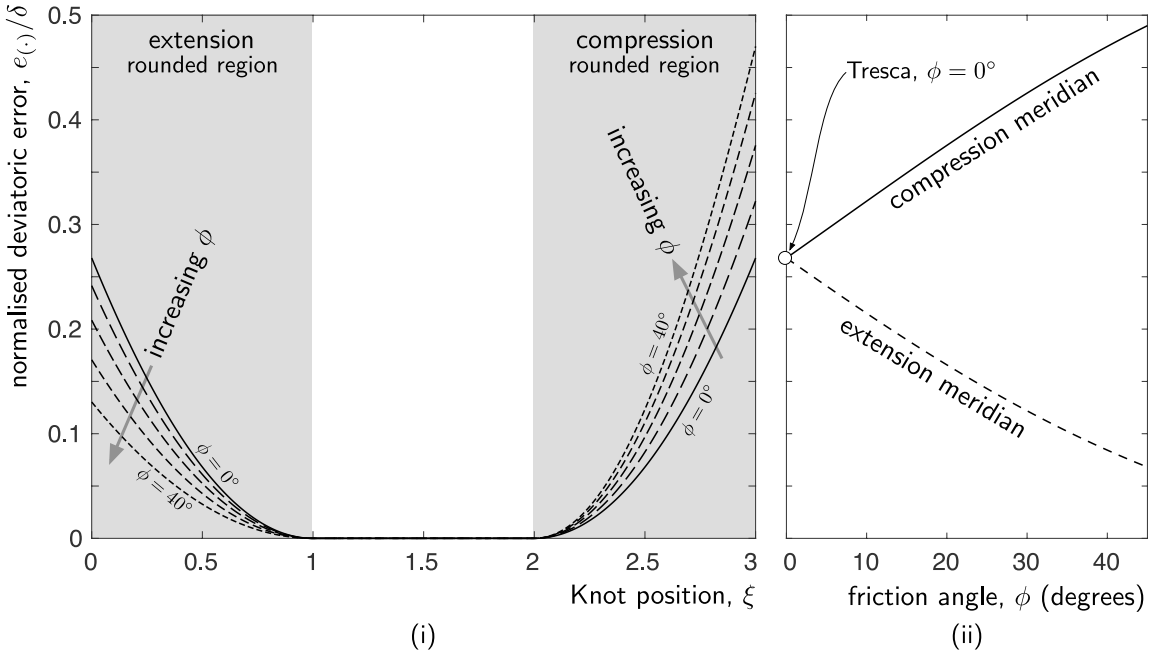

Figure 8: M-C errors associated with the rounded meridians: (i) normalised error versus local knot position for $\phi = 0°$, $10°$, $20°$, $30°$ and $40°$ and (ii) maximum normalised error versus friction angle for the compression and extension meridians.

4.2. Material point investigations

Before analysing some boundary problems we will first investigate the performance of the non-associated plastic flow NURBS plasticity framework at a material point (or stress-strain) level. In all cases two subdivisions (see Coombs et al. [11] for details) were applied before the bE stress return algorithm and n_d was set to 5 for the yield function estimation

resulting in 25 points being checked on the yield surface to determine if the stress state was undergoing elastic or elasto-plastic behaviour.

4.2.1. Drucker-Prager error analysis

This section analyses the errors associated with the implicit stress integration algorithm for a perfect plasticity D-P yield surface with non-associated flow. The material had a Young's modulus of 100Pa and a Poisson's ratio of 0.2. The cohesion was set to 0.49Pa, the friction angle to $\phi = \pi/9$ (20° degrees) and the final 0.1Pa of the yield surface apex was rounded[4]. The errors associated with the stress return algorithm were evaluated using dilation angles of $\pi/18$ and $\pi/36$ (10° and 5° degrees).

The stress state was initially located on the shear meridian in one of the sextants of stress space with a hydrostatic stress of $\zeta = 0$kPa. This point was then subjected to a stress increment that took the trial stress state outside of the yield envelope. The space of trial states explored was $\rho_t/\rho_n \in [1, 6]$, where the t and n subscripts denote the trial and starting locations.

The errors associated with the trial state are shown in Figure 9, using the following normalised error measure

$$\text{error} = \frac{||\{\sigma_{\text{NURBS}}\} - \{\sigma_e\}||}{||\{\sigma_e\}||}, \tag{43}$$

where $\{\sigma_{\text{NURBS}}\}$ is the stress return location associated with the NURBS model and $\{\sigma_e\}$ is the *exact* stress return[5]. The errors associated with $\psi = \pi/18$ and $\psi = \pi/36$ are shown on the right and left of the thick black line, respectively. The starting point for $\psi = \pi/18$ is shown by the white-shaded circle whereas the red-shaded circle is the starting point for the $\psi = \pi/36$ analysis.

Although errors of almost 20% are present in the model, exactly the same level of errors are observed in the D-P yield surface integrated with a conventional implicit stress integration procedure. As expected with any predictor-correction stress integration algorithm, the error increases as the tangential proportion of the stress increment increases. Errors also increase with increasing non-associativity, with $\psi = \pi/18$ having a maximum error of 1.66×10^{-1} whereas for the $\psi = \pi/36$ the maximum error was 1.92×10^{-1}, again this is due to the return path having a larger tangential component relative to the yield surface normal direction.

4.2.2. Mohr-Coulomb error analysis

This section analyses the errors associated with the implicit stress integration algorithm for a perfect plasticity M-C yield surface with associated and non-associated flow. The

[4]Note that although the apex of the yield surface was rounded, not stress states returned to the rounded part of the yield surface in this analysis.

[5]The exact stress state was approximated by using a conventional implicit stress return algorithm for the D-P model with the stress increment applied in 1000 sub steps.

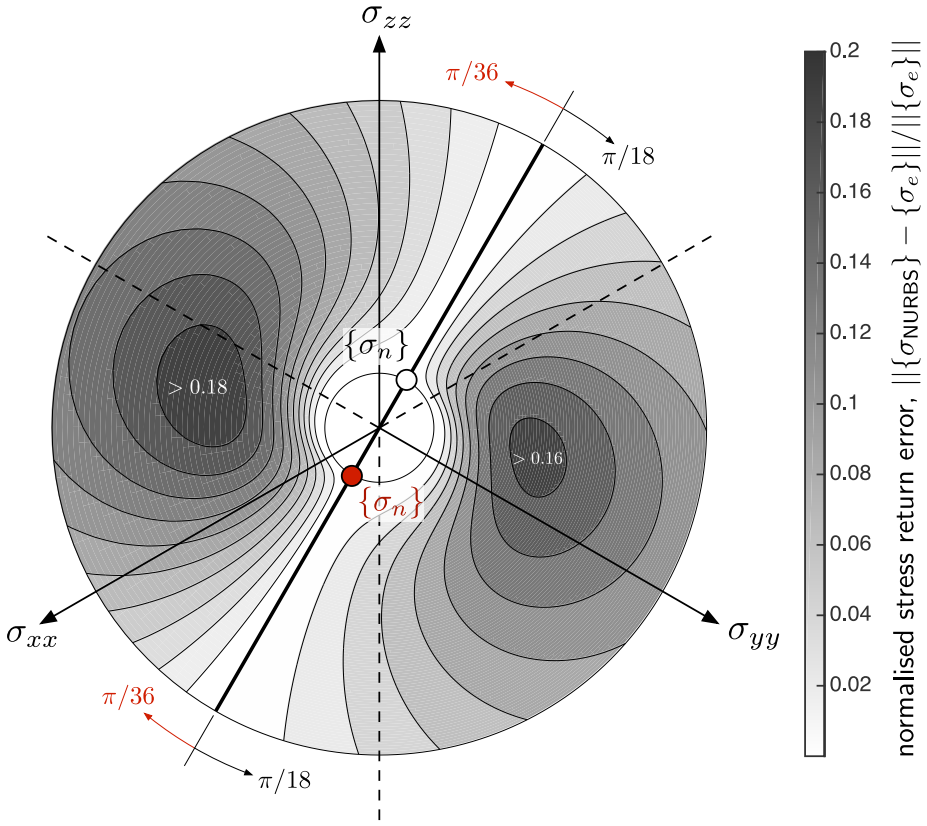

Figure 9: Stress return error analysis for D-P with non-associated flow with $\psi = \pi/18$ and $\psi = \pi/36$. The inner circle shows a deviatoric section through the yield surface and the white and red filled circles the starting points for the $\psi = \pi/18$ and $\psi = \pi/36$ error analyses, respectively.

material had a Young's modulus of 100Pa and a Poisson's ratio of 0.2. The cohesion was set to 0.49Pa and the friction angle to 20° and the final 0.1Pa of the yield surface apex was rounded. Figure 10 shows the errors in the NURBS stress return algorithm for the case of associated plastic flow. The M-C implementation of Clausen et al. [2] which explicitly includes the corners at the compression and shear meridians and the hydrostatic apex was taken as the reference solution for the stress integration algorithm Three different cases were examined, namely the comparison of a rounded NURBS surface with:

(A) $\delta = 0.1$ with [2] where the strain increment was applied in a single step;
(B) $\delta = 0.1$ with [2] where the strain increment was applied in 1,000 sub steps; and
(C) $\delta = 0.01$ with [2] where the strain increment was applied in 1,000 sub steps.

In all cases the strain increment was applied to the NURBS plasticity model in a single step. The errors associated with the stress return algorithm, as evaluated by (43), are shown over two sextants for the three cases in Figure 10. The thick black and red lines

show a section through the yield surface for $\delta = 0.1$ and $\delta = 0.01$, respectively. In all cases the stress state started at the intersection of the shear meridian and the yield surface with zero hydrostatic stress, as shown by the identified stress states in the figure.

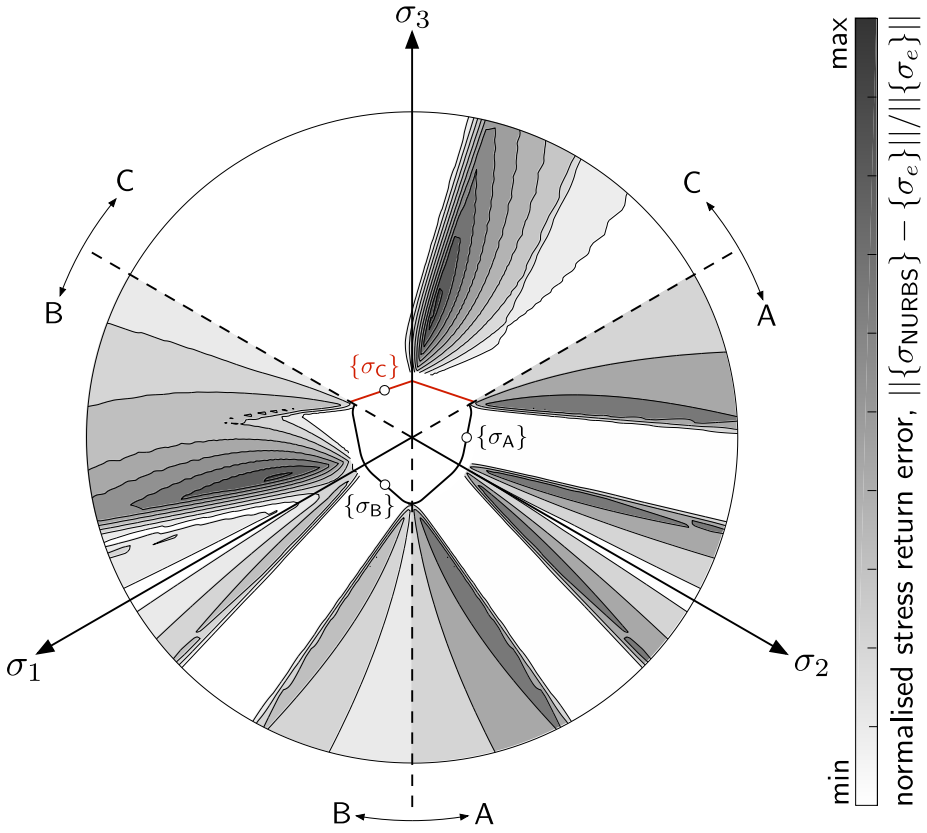

Figure 10: Stress return error analysis for M-C with associated plastic flow: (A) single step comparison of the NURBS surface with $\delta = 0.1$ and the true M-C surface, (B) 1,000 sub steps with $\delta = 0.1$ and (C) 1,000 sub steps with $\delta = 0.01$.

When comparing the true and rounded surfaces when subjected to the strain increment in a single step (region A in Figure 10) the non-zero errors exist in the trial regions that return to the rounded part of the yield surface. As expected from (42), the larger errors are associated with the compression meridian and symmetry is observed in the error distribution as the starting point is irrelevant when applying the strain increment in a single step. The maximum error for any trial point was 8.02×10^{-2}.

Subdividing the strain increment into 1,000 sub steps with the same level of local rounding (region B in Figure 10) gives a maximum error of 1.59×10^{-1} and this maximum error is located close to the extension meridian in the adjacent sextant to the initial stress state (the $\sigma_1 > \sigma_3 > \sigma_2$ sextant in Figure 10). Interestingly reducing the length of the

meridian rounding actually increases the maximum error in the stress return, with region C having a maximum error of 1.86×10^{-1}. This is because more points get trapped in the corner region that should actually return to the planar part of the yield surface. However, reducing the local rounding length does reduce the errors in the sextant of the initial stress state, as shown by the $\sigma_3 > \sigma_1 > \sigma_2$ sextant in Figure 10.

Table 1 gives the maximum errors for the M-C model with associated (grey shaded row) and non-associated plastic flow. As with the D-P model, the maximum error increases with increasing non-associativity and with decreasing δ. The M-C yield surface with sharp corners ($\delta = 0$) had the largest error for the reason explained above. The maximum number of N-R iterations for any of the trial stress states on any of the NURBS rounded M-C yield surfaces to find the updated stress state was 5.

Table 1: Maximum stress return errors for M-C with non-associated plastic flow, where n is the number of sub-steps and the letters A, B and C correspond to the same combinations of meridian rounding and sub-steps as used in Figure 10.

ϕ	ψ	A $\delta = 0.1$, $n = 1$	B $\delta = 0.1$, $n = 1000$	C $\delta = 0.01$, $n = 1000$	true M-C [2] $\delta = 0$, $n = 1000$
20°	20°	0.80×10^{-1}	1.59×10^{-1}	1.86×10^{-1}	1.92×10^{-1}
20°	10°	0.96×10^{-1}	2.18×10^{-1}	2.41×10^{-1}	2.43×10^{-1}
20°	5°	1.06×10^{-1}	2.58×10^{-1}	2.74×10^{-1}	2.79×10^{-1}
20°	2.5°	1.13×10^{-1}	2.91×10^{-1}	3.03×10^{-1}	3.05×10^{-1}
20°	0°	1.19×10^{-1}	3.29×10^{-1}	3.36×10^{-1}	3.41×10^{-1}

4.3. Boundary value simulations

This section presents the results from boundary value simulations to demonstrate the performance of the proposed non-associated flow NURBS plasticity framework. In all cases two subdivisions (see Coombs et al. [11] for details) were applied before the bE stress return algorithm and n_d was set to 5 for the yield function estimation resulting in 25 points being checked on the yield surface to determine if the stress state was undergoing elastic or elasto-plastic behaviour.

4.3.1. Plane strain rigid footing

The first analysis is that of a 1m wide plane strain rigid footing displacing into a weightless 10m by 5m domain with a Young's modulus of $E = 1 \times 10^7$kPa and a Poisson's ratio of $\nu = 0.48$. The yielding of the material was governed by a perfect plasticity D-P yield envelope (9) with cohesion of $c = 490$kPa and a friction angle of $\theta = \pi/9$ (20° degrees). Dilation angles of 20° and 10° degrees were considered with the second case requiring a non-associated flow rule.

The problem was analysed using a mesh comprising of 135 eight-noded bi-quadratic quadrilateral elements integrated using reduced four-point quadrature. Due to symmetry only half of the problem was modelled and the mesh detail around the corner of the footing is shown in the inset figure. The mesh is the same as that used by [6, 8, 9, 11, 20], amongst others. A vertical displacement of 4mm was applied to the footing over 20 equal loadsteps.

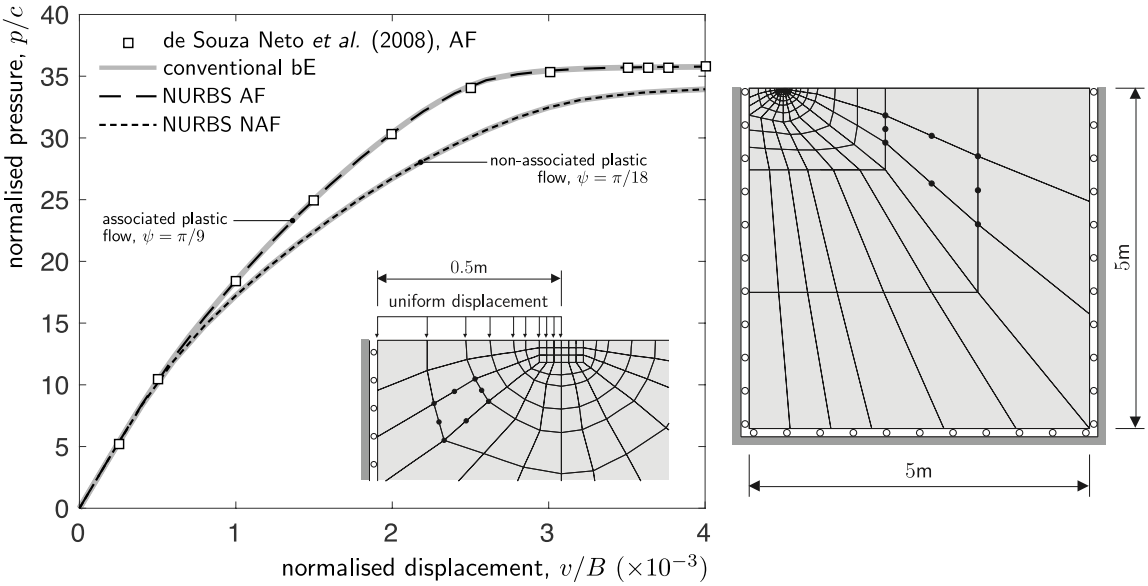

Figure 11: Rigid footing: normalised pressure versus displacement response with a D-P constitutive model.

The normalised pressure versus displacement response is shown in Figure 11 along with an inset figure showing the mesh detail around the rigid footing. B is the footing width, p is the footing pressure and v is the vertical displacement of the footing. The associate flow (AF) NURBS plasticity response (long dashed line) is compared with the result of de Souza Neto et al. [20] (discrete points) and that of a conventional backward Euler (bE) closest point projection implementation of the D-P yield surface (thick grey line). Excellent agreement is seen between the three results.

The non-associated flow result with $\psi = \pi/18$ (10° degrees) is also presented in Figure 11 for both the conventional bE (thick grey line) and the NURBS (short dashed line) models. As with the associated flow results, excellent agreement is seen between the two models. Figure 12 shows the deformed mesh around the footing for associated (top) and non-associated (bottom) plastic flow where the mesh has been shaded by the vertical displacement with dark grey being the maximum downwards displacement. The original mesh is shown by the fine dashed line and the displacements have been exaggerated by $\times 20$. The associated flow case exhibits excessive volumetric dilation in the region adjacent to the footing leading to unrealistic heaving of the ground surface. Reducing the dilation angle from $\pi/9$ (20°) to $\pi/18$ (10°) significantly reduces the heave leading to a more realistic deformed

surface profile.

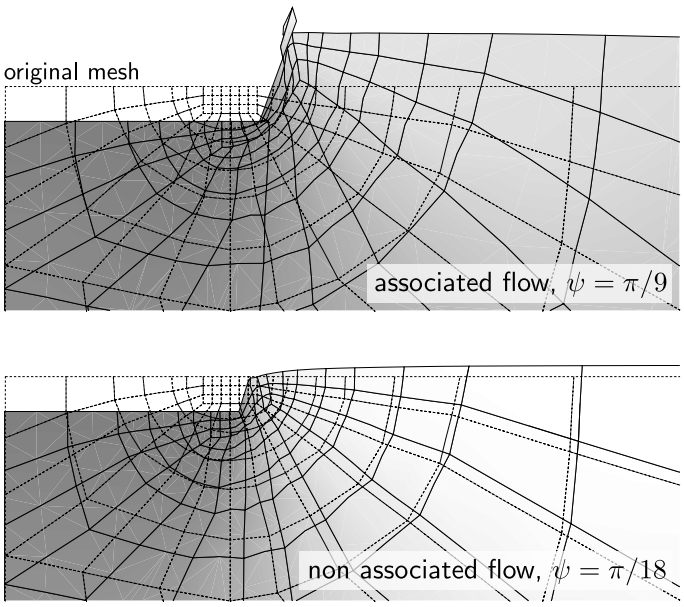

Figure 12: Rigid footing: deformed mesh for the associated (top) and non associated flow (bottom) D-P model with a $\times 20$ displacement magnification.

This rigid footing problem was also analysed using the M-C yield function. Figure 13 gives the normalised pressure versus displacement response for a perfect plasticity M-C model with cohesion of $c = 490$kPa and a friction angle of $\theta = \pi/9$ (20° degrees) for both associated and non-associated ($\psi = \pi/18$) plastic flow. The same mesh and elastic material properties used for the D-P analysis were used but in this case a displacement of 3mm was imposed using 20 equal displacement-controlled loadsteps. The results using the NURBS plasticity framework (discrete points) are presented alongside the implicit implementation of Clausen et al. [2] (solid grey lines). In both cases excellent agreement is seen between the two plasticity approaches and the normalised limit pressures agree well with the analytical limit pressure of $p/c = 14.84$, as shown by the dashed black line.

The rigid footing problem is now analysed using a mixture of D-P and M-C yield surfaces. The same mesh and elastic material properties as used in the previous analyses were used in this case and a displacement of 3mm was imposed using 20 equal displacement-controlled loadsteps. The different material models were randomly assigned at an element level and the distribution of the different constitutive models is shown in Figure 14 where the white and grey elements represent the D-P and M-C models, respectively. Only the NURBS information changed in order to simulate the different materials and the underlying numerics for the stress integration was the same in all cases. Both the M-C and D-P yield surfaces had a cohesion of $c = 490$kPa and a friction angle of $\theta = \pi/9$ (20° degrees).

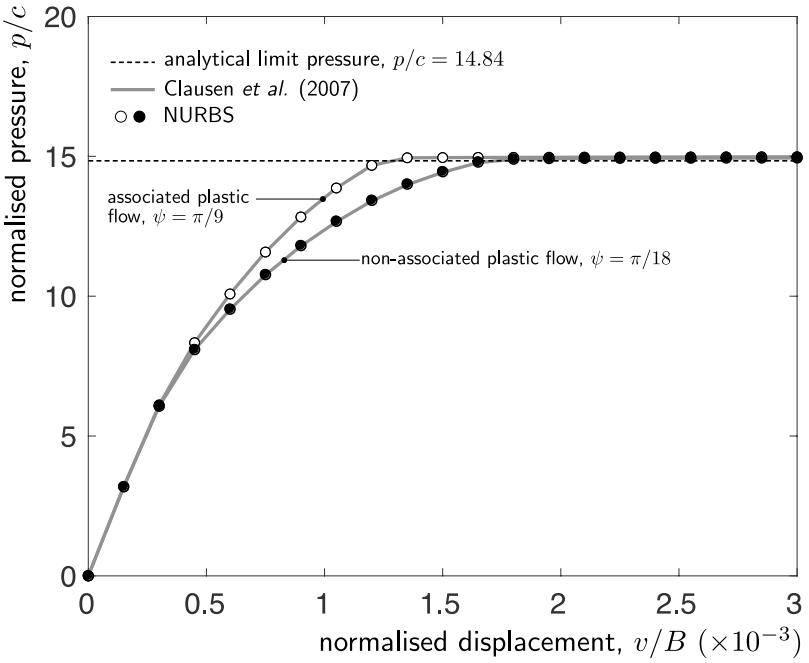

Figure 13: Rigid footing: normalised pressure versus displacement response with a M-C constitutive model.

Figure 15 shows the normalised pressure versus displacement response for this distribution of constitutive models with associated and non-associated ($\psi = \pi/18$) plastic flow. The responses when all of the elements used associated flow M-C and D-P models are also shown using dashed lines. The mixed constitutive model associated flow simulation has the potential to predict a response in the grey-shaded region of the figure depending on the number, and the distribution, of the elements using the different material models. As with the previous analyses, the NURBS plasticity response, shown by the discrete points, is compared with a conventional bE implementation and excellent agreement is seen for both for the associated flow and non-associated flow simulations.

4.3.2. Finite deformation cavity expansion

This section presents the finite deformation expansion of a cylindrical cavity under internal pressure. The problem was modelled using an updated Lagrangian finite element formulation with the following assumptions:

1. multiplicative decomposition of the deformation gradient into elastic and plastic components;
2. linear behaviour between Kirchhoff stress and elastic logarithmic strain; and
3. exponential map of the plastic flow.

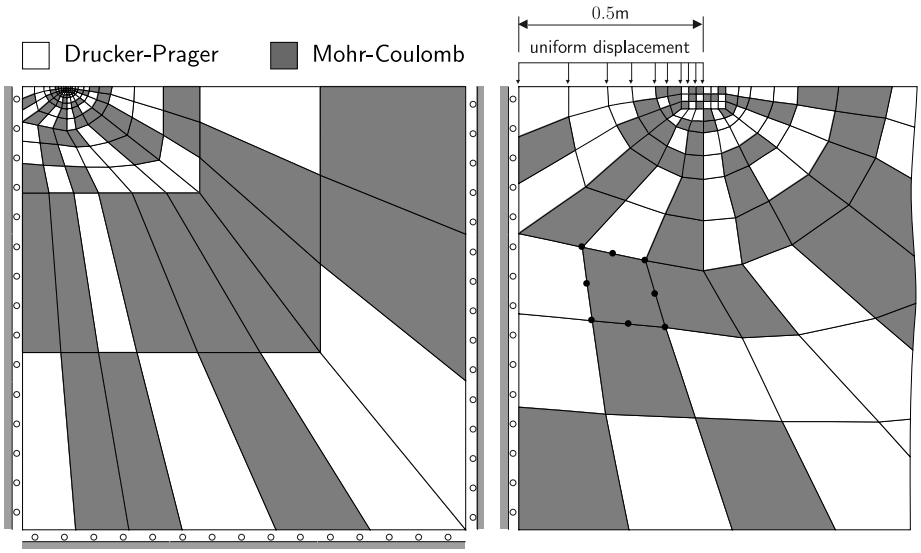

Figure 14: Rigid footing: constitutive model distribution over the finite element mesh, where the white and grey elements are represented using the D-P and M-C models, respectively.

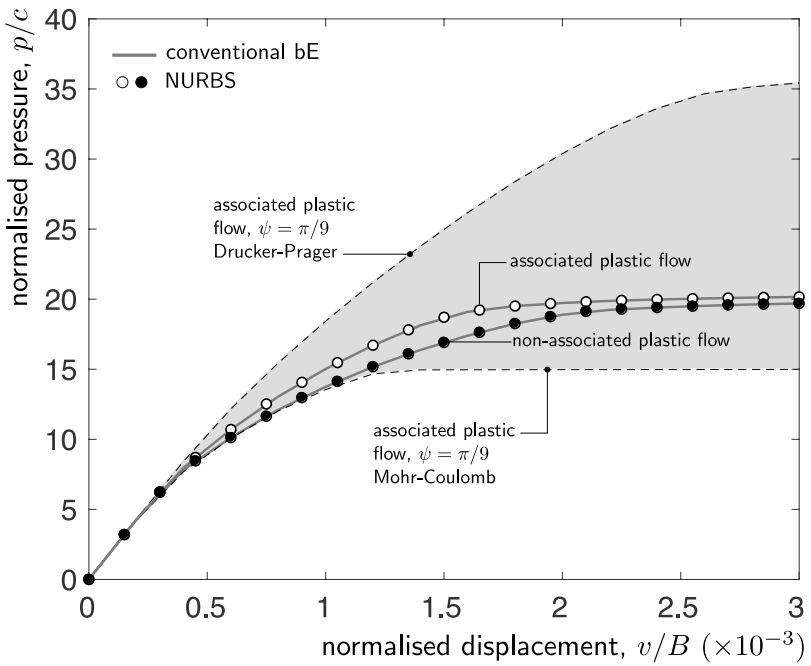

Figure 15: Rigid footing: normalised pressure versus displacement response with a mixture of D-P and M-C constitutive models.

The combination of these assumptions allows the infinitesimal strain format of stress integration algorithms to be maintained whilst extending the boundary value analysis to include finite deformation mechanics. See Coombs [4] for details of the large deformation formulation adopted in this paper.

The problem was modelled using a two-dimensional axisymmetric finite element code and had an inner radius of 1m and a fixed outer radius of 2km (to approximate an infinite domain). The inner radius, a_0, was expanded to 5m using 20 equal displacement-controlled loadsteps. The perfect plasticity M-C material had the following material parameters: Young's modulus of 100MPa, Poisson's ratio of 0.3, cohesion of 70kPa and a friction angle of $\pi/9$ (20°). Dilation angles of $\pi/9$ (20°), $\pi/18$ (10°) and 0 were considered. 150 fully-integrated eight-noded elements were used to analyse the problem and the size of the elements were progressively increased by a factor 1.1 from the inner to the outer surface (the inner and outer elements had radial lengths of 0.124mm and 182m, respectively). The analytical solution for this problem, assuming perfect plasticity M-C constitutive behaviour, was given by Yu and Houlsby [23].

Figure 16 shows the normalised internal pressure versus normalised radius response for the three dilation angles, where p is the internal pressure and a the current radius. The response of the NURBS plasticity model is shown by discrete points with the dilation angles of $\psi = 20°$, 10° and 0° being represented using white, grey and black filled circles respectively. The analytical solution given by Yu and Houlsby [23] is shown by the dashed black lines. The NURBS plasticity framework shows good agreement with the analytical solution for all of the dilation angles.

Table 2 gives the global Newton-Raphson (N-R) residual for loadsteps 1, 2, 3, 19 and 20 with $\psi = \pi/18$. The global tolerance was 1×10^{-06} and the maximum number of iterations for any loadstep was 5. The data presented in the table shows quadratic (or near quadratic) convergence of the global out of balance force, demonstrating the correct implementation of the algorithmic consistent tangent for large deformation elasto-plasticity.

Table 2: Finite deformation cavity expansion: global N-R iteration residuals for loadsteps 1, 2, 3, 19 and 20 with $\psi = \pi/18$. The convergence tolerance was 1×10^{-06}.

	loadstep				
NR it.	1	2	3	19	20
1	3.548×10^{-01}	1.645×10^{-01}	8.019×10^{-02}	3.549×10^{-03}	3.283×10^{-03}
2	6.375×10^{-01}	5.050×10^{-03}	1.084×10^{-03}	1.260×10^{-06}	9.958×10^{-07}
3	2.414×10^{-02}	1.819×10^{-06}	3.129×10^{-07}	3.817×10^{-11}	-
4	4.566×10^{-05}	2.585×10^{-10}	-	-	-
5	6.581×10^{-10}	-	-	-	-

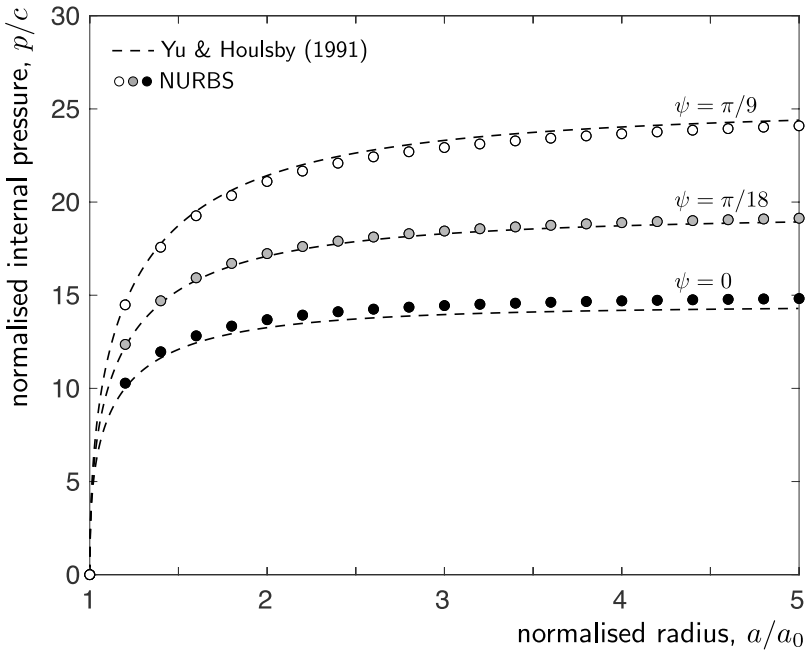

Figure 16: Finite deformation cavity expansion: expansion versus normalised internal pressure with a M-C constitutive model.

5. Conclusions

This paper has presented for the first time an extension of the NURBS plasticity framework of Coombs et al. [11] to include non-associated plastic flow. Information regarding the shape and size of the yield and plastic potential surfaces is stored at control points covering one sextant of stress space. This allows any smooth isotropic convex yield surface to be included within the plasticity formulation without modification of the numerics used for the stress integration. Within this, the implicit backward Euler stress update procedure contains three unknowns, namely the local position of the updated stress state on the yield surface and the updated hardening parameter. Therefore, introducing non-associated flow does not increase the number of unknowns in the stress integration algorithm as compared to the associated flow NURBS hardening formulation of Coombs and Ghaffari Motlagh [10]. In addition, when solving for these unknowns the current estimate for the updated stress state remains on the yield envelope and satisfies the consistency condition throughout the process. This results in a stable stress integration algorithm as, unlike in conventional closest point projection schemes, the stress state cannot be trapped in a local minimum or converge to an axillary surface outside of the true yield envelope (see [6] for more information on the impact of the form of the yield function on the stability of the bE stress integration process).

Unlike previous attempts to extend the NURBS plasticity framework to non-associated

flow, in this paper the geometry of the plastic potential surface is represented at the control points. This guarantees the ability to recover associated plastic flow for any surface. This is not possible when specifying the flow direction at the control points due to the presence of a cross product in the yield surface normal.

This paper has also proposed a new method to estimate if a trial stress state in inside (elastic) or outside (elasto-plastic) of the yield surface. This reduces the computational cost of the constitutive model as the closest point to the yield envelope only needs to be determined for those stress states undergoing elasto-plastic material behaviour.

The numerical examples included in this paper have quantified the errors associated with the stress integration process for both the Drucker-Prager and Mohr-Coulomb yield envelopes and where possible the maximum errors associated with yield surface smoothing have been specified analytically. The performance of the plasticity framework has also been demonstrated through a number of small strain and finite deformation finite element analyses where analytical or existing numerical results exist. Within this, the correct derivation and implementation of the algorithmic tangent has been confirmed through the convergence rate of the global out of balance force residual.

The key extension provided by this paper is that the evolution of plastic strain is decoupled from the yield surface normal. This allows the plasticity formulation to model a more diverse range of material behaviour and, in the case of frictional plasticity, predict a more realistic volumetric response, avoiding the excessive dilation seen with associated plastic flow.

Acknowledgements

This work was supported by the Engineering and Physical Sciences Research Council [grant number EP/M017494/1].

References

[1] A. Anandarajah, Computational methods in Elasticity and Plasticity: Solids and Porus Media, Springer, 2010.

[2] J. Clausen, L. Damkilde, L. Andersen, An efficient return algorithm for non-associated plasticity with linear yield criteria in principal stress space, Computers & Structures 85 (2007) 1795–1807.

[3] M. Coelho, D. Roehl, K.U. Bletzinger, Material model based on nurbs response surfaces, Applied Mathematical Modelling 51 (2017) 574 – 586.

[4] W.M. Coombs, Finite deformation of particulate geomaterials: frictional and anisotropic Critical State elasto-plasticity, Ph.D. thesis, Durham University, 2011.

[5] W.M. Coombs, Hardening and non-associated flow NURBS plasticity, in: E. Oñate, D. Owen, D. Peric, M. Chiumenti (Eds.), COMPLAS 2017: XIV International Conference on Computational Plasticity: Fundamentals and Applications, Barcelona, Spain, pp. 363–372.

[6] W.M. Coombs, R.S. Crouch, Algorithmic issues for three-invariant hyperplastic critical state models, Computer Methods in Applied Mechanics and Engineering 200 (2011) 2297–2318.

[7] W.M. Coombs, R.S. Crouch, Non-associated reuleaux plasticity: analytical stress integration and consistent tangent for finite deformation mechanics, Computer Methods in Applied Mechanics and Engineering 200 (2011) 1021–1037.

[8] W.M. Coombs, R.S. Crouch, C.E. Augarde, Reuleaux plasticity: analytical backward Euler stress integration and consistent tangent, Computer Methods in Applied Mechanics and Engineering 199 (2010) 1733–1743.

[9] W.M. Coombs, R.S. Crouch, C.E. Heaney, Observations on Mohr-Coulomb plasticity under plane strain, Journal of Engineering Mechanics 139 (2013) 1218–1228.

[10] W.M. Coombs, Y. Ghaffari Motlagh, NURBS plasticity: yield surface evolution and implicit stress integration for isotropic hardening, Computer Methods in Applied Mechanics and Engineering 324 (2017) 204–220.

[11] W.M. Coombs, O.A. Petit, Y. Ghaffari Motlagh, NURBS plasticity: Yield surface representation and implicit stress integration for isotropic inelasticity, Computer Methods in Applied Mechanics and Engineering 304 (2016) 342 – 358.

[12] J.A. Cottrell, T.J.R. Hughes, Y. Bazilevs, Isogeometric Analysis: Toward Integration of CAD and FEA, Wiley, New York, 2009.

[13] R.S. Crouch, H. Askes, T. Li, Analytical CPP in energy-mapped stress space: application to a modified Drucker-Prager yield surface, Computer Methods in Applied Mechanics and Engineering 198 (2009) 853–859.

[14] D. Drucker, W. Prager, Soil mechanics and plastic analysis or limit design, Quart. Appl. Math 10 (1952) 157–164.

[15] R. Mises, Mechanik der festen krper im plastisch-deformablen zustand, Gott Nach Math Phys Kl (1913) 582–592.

[16] L. Piegl, W. Tiller, The NURBS book, Springer Science & Business Media, 2012.

[17] M. Safaei, M.G. Lee, W.D. Waele, Evaluation of stress integration algorithms for elastic-plastic constitutive models based on associated and non-associated flow rules, Comput. Meth. Appl. Mech. Engrg. 295 (2015) 414–445.

[18] J.C. Simo, T.J.R. Hughes, Computational inelasticity, Springer, New York, 1998.

[19] J.C. Simo, R.L. Taylor, Consistent tangent operators for rate-independent elastoplasticity, Computer Methods in Applied Mechanics and Engineering 48 (1985) 101–118.

[20] E.A. de Souza Neto, D. Perić, D.R.J. Owen, Computational methods for plasticity: Theory and applications, John Wiley & Sons Ltd, 2008.

[21] H. Tresca, Memoire sur l'coulement des corps solides, Mmoires prsents par divers savants l'Acadmie Royale des Sciences de l'Institut de France (1872) 75–135.

[22] M. Wilkins, Calculation of elastic-plastic flow, in: S. Fernback, M. Rotenberg (Eds.), Methods of Computational Physics, volume 3.

[23] H. Yu, G. Houlsby, Finite cavity expansion in dilating soils: loading analysis, Geotechnical 41 (1991) 173–183.

[24] M.h. Yu, Advances in strength theories for materials under complex stress state in the 20th century, Appl. Mech. Rev. 55 (2002) 169–218.

Appendix A. Shear components and stress transformation

The constitutive model presented in this paper has been expressed in principal form. It is therefore necessary to detail the mapping of this model into generalised 6-component space. However, before this can be achieved it is necessary to specify the shear components of the algorithmic stiffness matrix so these can also be mapped to generalised stress space.

The shear terms of the modified elastic stiffness matrix are given by

$$[D_G^c] = [A_G][D_G^e], \tag{A.1}$$

where $[D_G^e]$ is a three-by-three matrix containing the shear components of the elastic stiffness matrix, the modification matrix for the shear components is given by [2]

$$[A_G] = \begin{bmatrix} 1 + \frac{\Delta\sigma_1^p - \Delta\sigma_2^p}{\sigma_1^r - \sigma_2^r} & 0 & 0 \\ 0 & 1 + \frac{\Delta\sigma_1^p - \Delta\sigma_3^p}{\sigma_1^r - \sigma_3^r} & 0 \\ 0 & 0 & 1 + \frac{\Delta\sigma_2^p - \Delta\sigma_3^p}{\sigma_2^r - \sigma_3^r} \end{bmatrix}. \tag{A.2}$$

The stiffness matrix used in (A.4) is therefore

$$[D] = \begin{bmatrix} [D^{alg}] & [0] \\ [0] & [D_G^c] \end{bmatrix}, \tag{A.3}$$

where [0] is a three-by-three matrix full of zeros and $[D^{alg}]$ is the principal elastic stiffness matrix from (37).

The following relations can be used to transform between six-component and principal stress and strain space

$$\{\hat{\sigma}\} = [Q]^T \left\{ \begin{array}{c} \{\sigma\} \\ \{0\} \end{array} \right\}, \qquad \{\hat{\varepsilon}\} = [Q]^{-1} \left\{ \begin{array}{c} \{\varepsilon\} \\ \{0\} \end{array} \right\} \qquad \text{and} \qquad [\hat{D}] = [Q]^T [D][Q], \quad \text{(A.4)}$$

where $(\hat{\cdot})$ denotes the six-component stress and strain quantities. The transformation matrix is given by

$$[Q] = \left[\begin{array}{cccccc} (q_1)^2 & (q_2)^2 & (q_3)^2 & q_1 q_2 & q_2 q_3 & q_3 q_1 \\ (q_4)^2 & (q_5)^2 & (q_6)^2 & q_4 q_5 & q_5 q_6 & q_6 q_4 \\ (q_7)^2 & (q_8)^2 & (q_9)^2 & q_7 q_8 & q_8 q_9 & q_9 q_7 \\ 2q_1 q_4 & 2q_2 q_5 & 2q_3 q_6 & q_1 q_5 + q_4 q_2 & q_2 q_6 + q_5 q_3 & q_3 q_4 + q_6 q_1 \\ 2q_4 q_7 & 2q_5 q_8 & 2q_6 q_9 & q_4 q_8 + q_7 q_5 & q_5 q_9 + q_8 q_6 & q_6 q_7 + q_9 q_4 \\ 2q_7 q_1 & 2q_8 q_2 & 2q_9 q_3 & q_7 q_2 + q_1 q_8 & q_8 q_3 + q_2 q_9 & q_9 q_1 + q_3 q_7 \end{array} \right], \quad \text{(A.5)}$$

where the components q_i are associated with the trial elastic strain eigenvectors

$$[q] = \left[\begin{array}{ccc} q_1 & q_4 & q_7 \\ q_2 & q_5 & q_8 \\ q_3 & q_6 & q_9 \end{array} \right]. \quad \text{(A.6)}$$

Appendix B. Jacobian matrix

The components of the Jacobian matrix, $[\partial r/\partial x]$, required for the backward Euler stress integration algorithm (30) are

$$\frac{\partial r_1}{\partial \eta} = -(S_{,\eta})_i (g_{,\eta})_i + (\varsigma_i^t - \varsigma_i^n)(g_{,\eta\eta})_i, \tag{B.1}$$

$$\frac{\partial r_1}{\partial \zeta} = -(S_{,\zeta})_i (g_{,\eta})_i + (\varsigma_i^t - \varsigma_i^n)(g_{,\eta\zeta})_i, \tag{B.2}$$

$$\frac{\partial r_1}{\partial h} = -(S_{,h})_i (g_{,\eta})_i, \tag{B.3}$$

$$\frac{\partial r_2}{\partial \eta} = -(S_{,\eta})_i (g_{,\zeta})_i + (\varsigma_i^t - \varsigma_i^n)(g_{,\zeta\eta})_i, \tag{B.4}$$

$$\frac{\partial r_2}{\partial \zeta} = -(S_{,\zeta})_i (g_{,\zeta})_i + (\varsigma_i^t - \varsigma_i^n)(g_{,\zeta\zeta})_i, \tag{B.5}$$

$$\frac{\partial r_2}{\partial h} = -(S_{,h})_i (g_{,\zeta})_i, \tag{B.6}$$

$$\frac{\partial r_3}{\partial \eta} = -(\tilde{h}_{,\Delta\varepsilon^{\mathrm{p}}})_i (\Delta\varepsilon^{\mathrm{p}}{}_{,\eta})_i, \tag{B.7}$$

$$\frac{\partial r_3}{\partial \zeta} = -(\tilde{h}_{,\Delta\varepsilon^{\mathrm{p}}})_i (\Delta\varepsilon^{\mathrm{p}}{}_{,\zeta})_i \qquad \text{and} \tag{B.8}$$

$$\frac{\partial r_3}{\partial h} = 1 - (\tilde{h}_{,\Delta\varepsilon^{\mathrm{p}}})_i (\Delta\varepsilon^{\mathrm{p}}{}_{,h})_i. \tag{B.9}$$

See Piegl and Tiller [16] for efficient methods of calculating the first derivatives of the NURBS basis functions. The derivative of the yield surface respect to the hardening function is

$$(S_{,h})_i = \frac{S_i}{h}. \tag{B.10}$$

The derivative of the plastic strain increment with respect to h is

$$(\Delta\varepsilon^{\mathrm{p}}{}_{,h})_i = -C^{\mathrm{e}}_{ij} T^{-1}_{jk} (\varsigma^n{}_{,h})_k \tag{B.11}$$

and the derivatives of the plastic strain increment with respect to η and ζ are

$$(\Delta\varepsilon^{\mathrm{p}}{}_{,\eta})_i = -C^{\mathrm{e}}_{ij} T^{-1}_{jk} (S_{,\eta})_k \qquad \text{and} \qquad (\Delta\varepsilon^{\mathrm{p}}{}_{,\zeta})_i = -C^{\mathrm{e}}_{ij} T^{-1}_{jk} (S_{,\zeta})_k. \tag{B.12}$$

The derivative of the hardening function with respect to the plastic strain increment is

$$(\tilde{h}_{,\Delta\varepsilon^{\mathrm{p}}})_i = \alpha \frac{\Delta\varepsilon^{\mathrm{p}}_i}{||\Delta\varepsilon^{\mathrm{p}}||} \tag{B.13}$$

Note the relative magnitudes of the residuals in (27), with the first two residuals will be of the order of stress squared and the third close to unity. Normalising the first two residuals (and the appropriate entries in the Jacobian matrix) with respect to Young's modulus reduces the potential for ill conditioning of the Jacobian matrix.